

Spacer defined intrinsic multiple patterning

Sophia K. Laney,^{1‡} Tao Li,^{1‡} Martyna Michalska,^{1‡} Francisco Ramirez,¹ Mark Portnoi,¹ Junho Oh,² Manish K. Tiwari,^{2,3} Iain G. Thayne,⁴ Ivan P. Parkin,⁵ and Ioannis Papakonstantinou^{1}*

¹ Photonic Innovations Lab, Department of Electronic & Electrical Engineering, University College London, Torrington Place, London WC1E 7JE, UK

² Nanoengineered Systems Laboratory, Department of Mechanical Engineering, University College London, Torrington Place, London WC1E 7JE, UK

³ Wellcome/EPSRC Centre for Interventional and Surgical Sciences (WEISS), University College London, London, W1W 7TS, UK

⁴ James Watt School of Engineering, University of Glasgow, Glasgow G12 8LT

⁵ Department of Chemistry, University College London, Torrington Place, London WC1E 7JE, UK

KEYWORDS: nanofabrication, multiple patterning, binary/hierarchical nanostructures, nanotubes, atomic layer deposition, broadband antireflection

ABSTRACT: Periodic nanotube arrays render enhanced functional properties through their interaction with light and matter, but to reach optimal performance for technologically prominent applications, *e.g.*, wettability or photonics, structural fine-tuning is essential. Nonetheless, a universal and scalable method providing independent dimension control, high aspect-ratios, and the prospect of further structural complexity, remains unachieved. Here, we answer this need through an atomic layer deposition (ALD)-enabled multiple patterning. Unlike previous methods, the ALD-deposited spacer is applied *directly* on the pre-patterned target substrate material, serving as an etching mask to generate a multitude of *tailored nanotubes*. By concept iteration, we further realize concentric and/or binary nanoarrays in a number of industrially important materials such as silicon, glass, polymers. To demonstrate the achieved quality and applicability of the structures, we probe how nanotube fine-tuning induces broadband antireflection, and present a surface boasting extremely low reflectance of <1% across the wavelength range 300-1,050 nm.

The proliferation of interest in periodic nanostructured surfaces has driven significant advancements in nanofabrication techniques, leading to their successful implementation into energy storage devices,¹ solar cells,^{2,3} sensing,⁴ and special wetting surfaces.⁵ Whilst the collective interactions of many sub-components within an array, and the resultant surface properties are well studied for pillars, cones or holes, more complex designs allude to more exotic phenomena. For example, superior control over localisation of electromagnetic fields can be achieved,⁶⁻⁸ if only the complexity of sub-components is tuned adequately. In particular, nanotubes; hybrid structures of nano-holes within pillars that amalgamate the best

attributes from each (high surface area yet low solid fraction), are gaining significant attention due to their widespread applicability spanning solar cells,⁹ batteries,^{10,11} sensing/SERS,¹²⁻¹⁴ molecule delivery systems,¹⁵ smart surfaces,¹⁶ and nanocatalysis.¹⁷ Despite the progress to achieve nanotube arrays, expanding on their complexity (*e.g.*, concentric/binary structures) alongside advanced feature control and large-scale fabrication, remains a synthetic bottleneck.

Some advances have been made to address these shortcomings, like colloidal templating in combination with metal sputtering and reactive ion etching (RIE),^{18,19} and a recently reported multi-patterning technique.²⁰ Although the latter is scalable and harnesses nanometer-scale dimension control, shape tunability and binary structure generation is limited; yet desired in many applications, where subtle structural changes often drastically impact on overall performance.²¹ Latest advancements in binary nanoarray generation have emerged through anodic aluminum oxide templating, allowing highly controlled optimisation of morphology and/or material, but at the cost of complicated fabrication.⁶ Well-defined hollow nanostructures (*e.g.*: nanotubes, nanovolcanos) have been achieved *via* secondary electron lithography induced by ion-beam milling, however this too suffers from scalability.²² One method that has gained the attention of the semiconductor industry, is spacer defined double patterning (SDDP), which uses ALD instead of multistep lithographic processes to overcome the resolution limit and reduce fabrication steps, thus better complying with high volume manufacturing.²³⁻²⁵ In SDDP, a highly conformal ALD-deposited film-spacer is applied to a sacrificial pattern (photoresist or hard mask) and etched anisotropically so that the spacer sidewalls serve as an etching mask, resulting in a pitch half of the original. For 1D gratings,

SDDP is a well-established method, with double iterations often performed to further multiply pattern resolution.²³ However, despite the low process complexity, only few examples of SDDP onto 2D patterns (holes/pillars) to generate nanotubes – a morphology otherwise challenging to obtain – have been reported.^{17,26,27} Yet still, these demonstrations do not harness the full dimensional control, nor do they expand on the structural complexity through further iterations.

To that end, we present an alternative branch of ALD-assisted etching, namely *spacer defined intrinsic multiple patterning* (SDIMP), to generate wafer-scale tailored nanotubes, as well as complex nanoarrays.. Unlike previously reported spacer deposition on 2D-patterns, we first etch nanoholes or nanopillars of varying aspect-ratio (AR=1-6) into the target substrate material (Si or SiO₂), and directly deposit the Al₂O₃-spacer, as opposed to performing ALD earlier, on the photoresist/hard mask itself (Figure S1 further highlights the differences between SDDP and SDIMP). This generates intrinsic, rather than free-standing nanotubes which provides excellent control over pattern integrity and height. By virtue of a comprehensive mechanistic understanding, we first demonstrate independent control over nanotube dimensions; pitch/spacing, height, and diameter – already leading to binary nanoarrays, and also show structure replication into polymers. Advancing the control further, we tune the morphology; geometry, tapering and internal structuring. Furthermore, by performing a second SDIMP iteration, an expansive library of complex nanostructures can be achieved (Figure S2) and we demonstrate some as a proof-of-concept; fabricated in a large-scale yet straightforward manner. Finally, we illustrate photonics as one of the many potential applications, with an exemplar tailored nanotube array achieving efficient broadband

antireflection; <1%, 300-1,050 nm. Given the ability to engineer unlimited combinations of feature sizes and dimensions through one or more iterations, we envision SDIMP to be a general route for the fabrication of complex meta-nanostructures targeting applications in SERS and optical trapping, for instance.

RESULTS AND DISCUSSION

Spacer defined intrinsic multiple patterning. Figure 1 details the fabrication process of the silicon (Si; target material) nanotube arrays, which can have two distinct starting points; photoresist (PR) nanopillars (Figure 1a) or nanoholes (Figure 1b). The evolution of the structures (Step 1-6) is presented in a collection of scanning electron microscopy images (SEM; Figures S3-S5) which begins from the generation of PR pattern (Figure 1, Step 1), with detailed information on specific conditions/times/thicknesses/dimensions given in Tables S1-S4. A Si wafer with a thin layer of deposited glass (SiO_2) is coated with PR and then patterned *via* laser interference lithography to achieve periodically-ordered square or hexagonally close-packed PR nanopillars or nanoholes (LIL; Figure S6). Note, *any* lithographic method can be used to pattern the PR, thus enabling various pitches and geometric arrangements (periodic or non-periodic). Step 2 uses a fluorine (F) based RIE to register the pattern into the SiO_2 layer. This acts as a hard mask in Step 3 when chlorine (Cl) plasma is used to etch into Si (selectivity ~10:1) which, distinctive of SDIMP, permits the generation of intrinsic nanohole/pillars of high aspect-ratio greater than four. Step 4 involves ALD-coating the attained Si arrays in a layer of aluminium oxide (Al_2O_3 =spacer) of predetermined thickness (t). The subsequent RIE takes place in a single step, however to understand the mechanism, it is broken down into two parts; (i) a breakthrough etch which

acts to anisotropically remove a horizontal spacer layer equal to t , to attain exposed Si inside and outside a tube of Al_2O_3 (Step 5), and (ii) a selective etch using vertical spacer sidewalls as a mask (Step 6). Due to the high etch selectivity under Cl plasma ($>15:1$), evidenced in Figure 1f with an obtained selectivity ~ 20 , the Al_2O_3 -coated sidewalls etch more slowly than Si, thus enabling the transfer of the pattern into Si and the generation of high-aspect ratio nanotube arrays (where high AR at the nanoscale is defined as >1). Note, other RIE processes could be easily employed such as pseudo-Bosch recipe utilizing $\text{SF}_6/\text{C}_4\text{F}_8$ gases,²⁸ given the process is selective (Text S1). The etching proceeds until the mask consumption, or alternatively the residual spacer can be removed by hydrofluoric acid.

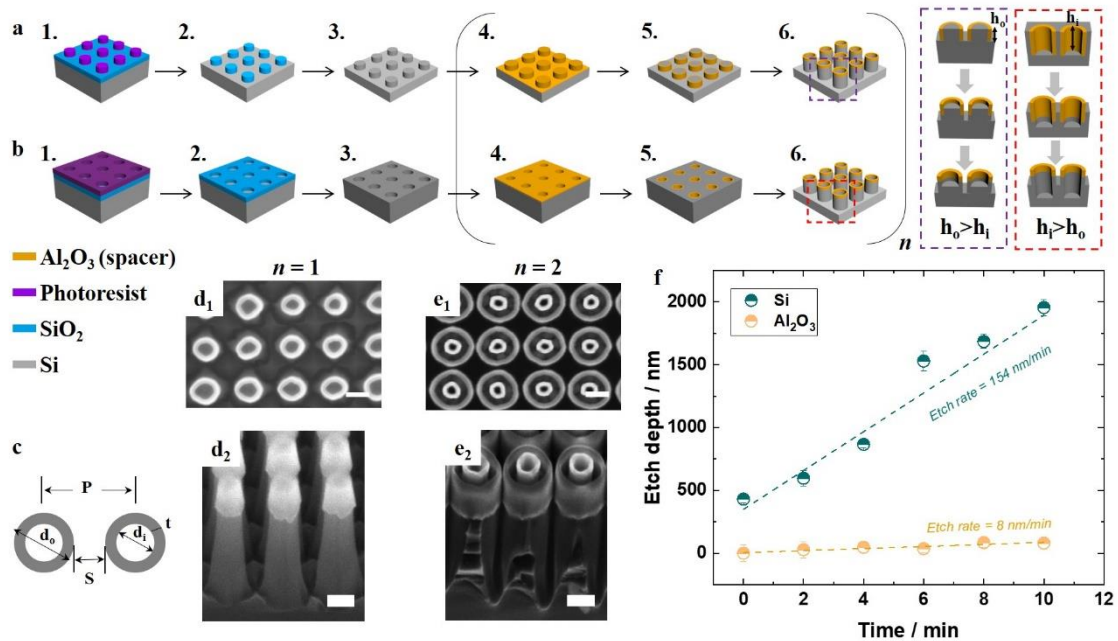


Figure 1. Nanotube fabrication process and tuning of the pitch and height. (a,b) Schematics of the fabrication process starting from photoresist pillars (a) or holes (b). From left to right: (Step 1) PR pattern; (Step 2) Etching the underlying SiO₂ layer using the PR mask; (Step 3)

Etching silicon using the SiO₂ as a hard mask; (Step 4) Depositing conformal layer of Al₂O₃ *via* ALD; (Step 5) Etching Al₂O₃ to consume horizontal deposition but leave vertical (sidewall) deposition; (Step 6) Etching into silicon using spacer-sidewalls as a hard mask [outer sidewalls of pillar (a) or inner sidewalls of hole (b)]; Steps 4-6 can be iterated n times to obtain numerous complex nanostructures. Schematics on the right-hand side illustrating the difference in inner and outer height (h_i and h_o , respectively) of the end nanotube when starting from a nanopillar array (purple) or nanohole array (red). (c) Top view schematic indicating the notation to describe nanotube arrays, where S =spacing, P =pitch, d_o =outer diameter, d_i =inner diameter, t =thickness of tube corresponding to ALD thickness. (d₁,e₁) Top view and (d₂,e₂) side view SEM images of nanostructures after one or two iterations (n=1,2). (f) Graph highlighting the selectivity of the process, with etch rates for Si (154 nm/min) and Al₂O₃ (8 nm/min) giving rise to a selectivity ~20 for an example nanotube array, originating from a pillar morphology. Scale bars = 200 nm.

The main criterion for SDIMP is to select materials with high etching contrast (selectivity) in an anisotropic RIE process (see Text S1 for more details)²⁹. To demonstrate this versatility, we show similar nanotube formation in glass using CHF₃/Ar chemistry during RIE with either PR or Al₂O₃ mask (Figure S7). Additionally, we show replication of the structure in photoresist *via* nanoimprint lithography (NIL), as well as generation of an inverse nanotube morphology with hierarchical features in polyurethane acrylate *via* soft lithography (Figure S8). These serve as examples for either further scaling-up (NIL) or to provide inspiration for additional applications requiring flexible substrates.

One SDIMP iteration – mechanism of control. To achieve designer complex nanostructures, the challenge lies in an effective control of each sub-dimension. We therefore begin with breaking down the levels of independent control attainable through one SDIMP iteration. First, we tune the nanostructure size (pitch/spacing, height, diameter) and then delve into a more advanced level of control over the morphology (geometry, tapering). We demonstrate further how, through intelligent design and collective tuning of features, additional complexity can be introduced. Further guidance on structural control is provided in Table S5.

The pitch (P , defined in Figure 1c) and spatial arrangement of the nanoarrays is dictated by the lithographic method used – here LIL – providing flexibility in defining this parameter. Two nanotube arrays of $P = 350$ and 560 nm are shown in Figure S9 demonstrating excellent pattern resolution of the end nanotube which is an attribute of the precise techniques involved: ALD and plasma etching. Similarly, the lithographic method determines the morphology of the PR; nanopillar or nanohole. By deliberately choosing one starting morphology, the relation between the outer and inner height of the tube (h_o and h_i , respectively) can be addressed, and the evolution is shown schematically on the right-hand side of Figure 1a. We monitor this evolution for exemplary nanotubes originating from nanopillars and nanoholes in Figures S3 and S4, respectively, where it can be seen that h_o becomes greater than h_i in a former case and $h_i > h_o$ in the latter. However, other factors such as RIE lag³⁰ (lower etching rates at smaller feature sizes and *vice versa*) can alter the expected evolution of h_o and h_i , as presented in Figure S4.

Whilst nanotubes of high aspect-ratio can be generated, with the highest AR of ~6 attained in this study (Figure S3f), low aspect-ratio 2D nanorings can also be realised. Independent control of the inner diameter is gained when starting from nanohole morphology and depositing Al₂O₃ of precise thickness (Figure 2a,c) with subsequent etching to generate the nanotubes (Figure 2b,d). Control of the outer diameter is equivalently obtained when starting from nanopillars with a possible extension towards connected or binary nanoarrays (Figure 2e,f), as a consequence of Al₂O₃ deposition when criterium of $t > (S/2)$ is met. Additionally, this enables a change in the spatial arrangement (Figure S2).

We now show more advanced control over the nanotube geometry, in addition to combining the acquired understanding to create more intricate structural changes. Unlike the PR mask, the robustness of the SiO₂ hard mask facilitates finer geometry tuning, as it withstands a wider range of RIE conditions. For example, it allows for achieving both circular and square nanoholes in Si (Figure 2g,i), by varying RIE power. The morphological change arises from angular ion distribution, whereby ions impact and scatter from the evolving feature.

Consequently, not only more angular (square) nanoholes are created, but also facets at the top of the hole and trenching at the base (see Figure S10), and this becomes more apparent with greater RIE power and longer process time.³¹ This additional level of flexibility and control carries through to the nanotube due to the conformal nature of ALD, allowing cylindrical or cuboid nanotubes to be formed (Figure 2h,j).

By taking advantage of the aforementioned tuning mechanisms, the discussed facet formation in the Si nanohole materialises as a crown structure. This feature can be further preserved and

transferred into the nanotube through (i) a thick layer of Al_2O_3 and (ii) mild post-ALD etching conditions, which also gives rise to outer sidewall tapering (Figure S11). The necessity for such a high degree of morphological control is critical for optical properties as

discussed in the Applications section.

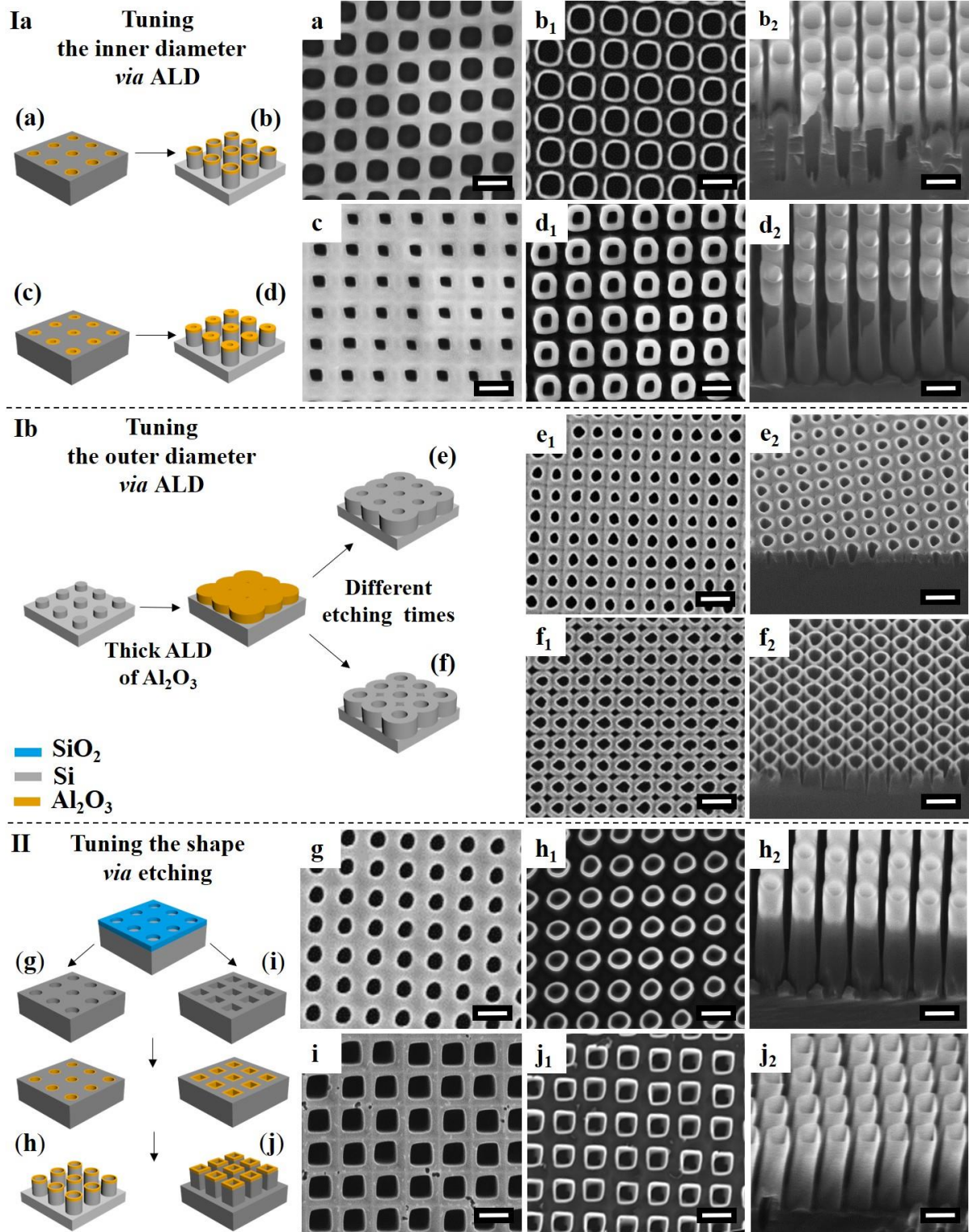


Figure 2. Fine-tuning the nanotube dimensions during one SDIMP iteration. SEM images (top views labelled as x or x_1 ; and 45° tilted labelled as x_2) demonstrating examples of how the shape of the tube can be tuned at different stages in the fabrication process. (Ia,Ib) Schematic and corresponding SEMs of tuning inner and outer diameter. (Ia) When starting from the same nanohole structure but differing in the ALD thickness; (a)=30 nm, (c)=90 nm, tubes with thinner (b) or thicker walls (d) are achieved. (Ib) When starting from the same pillars, coated with thick spacer layer, but differing in etching time, connected (e) or binary arrays (f) are generated. Note that thickness of deposited layer must correspond to at least half of the pillar spacing. (II) Schematic and corresponding SEMs of tuning the shape of nanostructures. When starting from the same SiO_2 hard mask, but altering the silicon etch conditions (coil/platen power and time), cylindrical (g) or square holes (i) are generated. The subsequent ALD process and etch results in cylindrical tubes (h) or cuboid tubes (j). Scale bar = 500 nm.

Two SDIMP iterations – complex structures. Unlike previously demonstrated spacer defined quadruple patterning (SDQP),²³ where the additional iteration requires a different spacer material, we repeat SDIMP in the same manner, providing a proof-of-concept of higher complexity structures created through multiple iterations. However, owing to the now more densely-confined features, the etching conditions may need an adjustment to converge to the same quality between iterations and prevent pattern distortions likely caused by high-energy ions reflecting off the greater surface area, for instance. As an example, we note non-equivalent roundness of the inner and outer rings of the concentric structures in Figure 3b, calculated to be 0.89 ± 0.06 and 0.95 ± 0.08 , respectively (where 1 corresponds to the perfect

circle). Here, we demonstrate some of the myriad of designs, and start from the same cylindrical nanotube array, but vary the thickness of the second ALD, to determine whether concentric or connected concentric nanotubes are formed (Figure 3b and 3c, respectively). Alternatively, by starting from a nanotube with a smaller inner radius and large spacing, the second ALD can result in nanotubes with an internal nanopillar (Figure 3e). Performing the second iteration on a structure such as the porous binary nanoarray in Figure 2f, enables extruding binary nanostructure to be achieved (Figure 3g).

Note also, through careful design, multilevel concentric structures can be fabricated by taking advantage of the inner/outer height difference of the starting nanotube: for $h_i > h_o$ see Figure 3h,i; alternatively, for $h_o > h_i$ see Figure S13. Also noteworthy in Figure 3i is the spatial arrangement (hexagonally-packed) and the glass (rather than silicon) substrate. This emphasises the fact that numerous exotic nanostructures can be achieved in different materials by simple and scalable means, by virtue of the countless ALD/RIE combinations, which we expand on in Figure S2 (nanostructure library) and Text S1. Our proof-of-concept demonstration of double SDIMP offers a simple route to generate highly complex structures with advanced control over feature sizes (sub-10 nm gaps; Figure S12), which we anticipate to attract great interest for application in optical trapping and SERS for instance, and we discuss it further in Text S2.^{32,33}

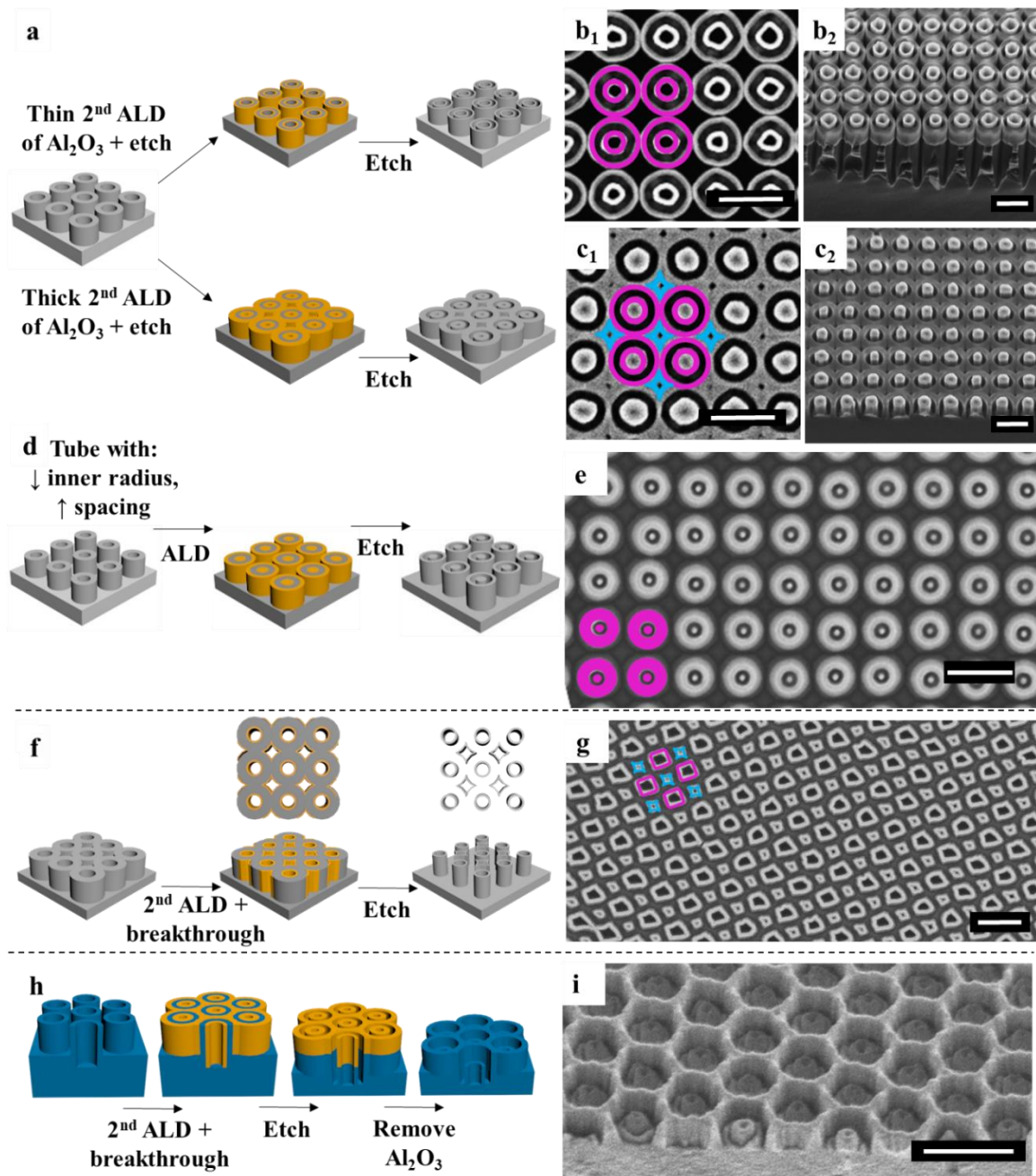


Figure 3. Exemplary complex structures by two SDIMP iterations. Schematics and corresponding SEM images show some of the possible structures when the second SDIMP process is conducted. Structural units are schematically depicted and bicolour refers to

morphologically-binary structures. (a) When starting from the same nanotube structure, but depositing a thinner or thicker spacer layer in the subsequent ALD and etch, concentric nanotubes (b) or connected concentric nanotubes (c) are generated. (d) When starting from a nanotube with a reduced inner radius and greater spacing, a nanotube with an internal pillar can be created (e). (f) When starting from connected nanotube arrays, the subsequent ALD and etch can generate extruding binary nanoarrays (g), note the schematic is simplified for the case where the inner tube is circular, as opposed to square which is seen in the corresponding SEM. (h) When starting from nanotubes with a greater inner depth than outer height, multilevel concentric structures are generated (i) and in this case have been fabricated in glass to emphasise the process versatility. Scale bars = 500 nm.

Applications – broadband antireflection. Antireflective properties imparted by silicon nanostructuring have been largely explored as a method to improve the light trapping efficiency in optoelectronic devices.^{9,34} Here, the enhanced material performance is typically attributed to the subwavelength features and the co-action of various mechanisms which include coupling with localized or waveguided photonic modes³⁵ in addition to the induced refractive index gradient between air and the substrate.³⁶ Whilst arrays comprising Si nanowires,³⁷ nanocones,³⁴ nanotips,³⁸ or nanotubes⁹ have shown a reduced reflection, typically one mechanism dominates; and furthermore, antireflection is only observed in partial regions of the solar spectrum ($\lambda \sim 250\text{-}2500$ nm). Because these structures hold a single geometrical feature, to achieve broadband antireflectance, a large AR (>30:1) is required^{38,39}; but at the cost of structure durability. An alternative path to render such

properties relies on expanding feature hierarchy,^{21,40} so that each feature now can interact with a specific part of the spectrum.

Therefore, both independent dimension control and the possibility to iterate our SDIMP method make it particularly suitable for the development of complex nanostructures with broadband antireflective properties. Here, as an example we show a nanotube array with subwavelength dimensions, additionally possessing crowned features at the top. Upon measurement of the fabricated surface (visually assessed as exceptionally black) using an integrating sphere (see Methods), we indeed find a very low reflectance of an average 1.0% between 350-550 nm and 0.7% for 550-1,050 nm, which translates to 0.9% overall (Figure 4c, magenta dashed line).

To elucidate the contribution of structural components to the high value of the measured antireflectance, we simulate four similar geometries with varying complexity (Figure 4c): straight-walled tube (black curve), tapered tube (red), tapered pillar with a top crown (orange), and tapered tube with a top crown (yellow). It is clear that with increasingly complex geometric features, the reflectance is further suppressed. For instance, the straight-walled tube array shows an average reflectance of 12.1% which is comparatively lower than that from a flat substrate, but still large compared to previously achieved nanostructured Si surfaces. By reshaping the tube through adding tapered sidewalls, the reflectance is significantly reduced across 500-900 nm wavelength range, and the average reflectance decreases to 5.1%. Removing the central hole and adding a top crown to the previous structure (orange curve) shows further improvements of the antireflective properties; lower

reflectance overall and on average 2.2% as compared to the previous cases. Finally, by adding a central hole to the previous structure to obtain a tapered tube with a top crown (yellow curve), light couples to the waveguiding modes into the tubular structure, achieving an extra reduction in reflectance (1.5% average). Further suppression of reflectance to the levels observed in the experiments (0.9%) could be attributed to the small roughness at the walls of the tubes (Figure 4b). We note that these findings corroborate well with the very recent study on the natural surfaces of the wings of papilionid butterflies²¹ where a 16-fold suppression of reflectance was similarly attributed to the existence of steep ridges surrounding a nanohole (crowned tapered nanostructures). Although the exact role of the size and shape of the hole in such structures is still under debate (with ambiguity regarding absorption management at non-normal incidence angle), it is clear that generally two shapes come into play – spherical and square, both of which can be attained by SDIMP.

Building on from our simulations, the electric field distribution of tapered tubes and tapered crown tubes (Figure 4d,e) indicate further that the top crown is a critical element to suppress the reflectance of light at small wavelengths (300-560 nm) as it allows for the efficient coupling of light into the structure. Numerical simulations at oblique angles of incidence for s and p polarisations (Figure S14) reveal that reflectance remains below 5% for angles as large as 50°, and most of the light at wavelengths 350-500 nm is being absorbed by the tubes before reaching the substrate. This shows that localized modes at the crown top and waveguided modes in the central hole are the major mechanisms contributing in this range. For longer wavelengths on the other hand, most absorption occurs within the substrate, which indicates that the structures act to gradually match the impedance between air and Si in this

spectral range. Through this example, concomitantly with the merits of other attainable complex structures by iterative SDIMP, we believe that our technology holds a great potential for future designs of perfect absorbers. Additionally, to the best of our knowledge, this represents the only reported synthetic analogue of ultra-black crowned tapered nanostructures similar to those found on the papilionid butterfly, further reinforcing potential of SDIMP.

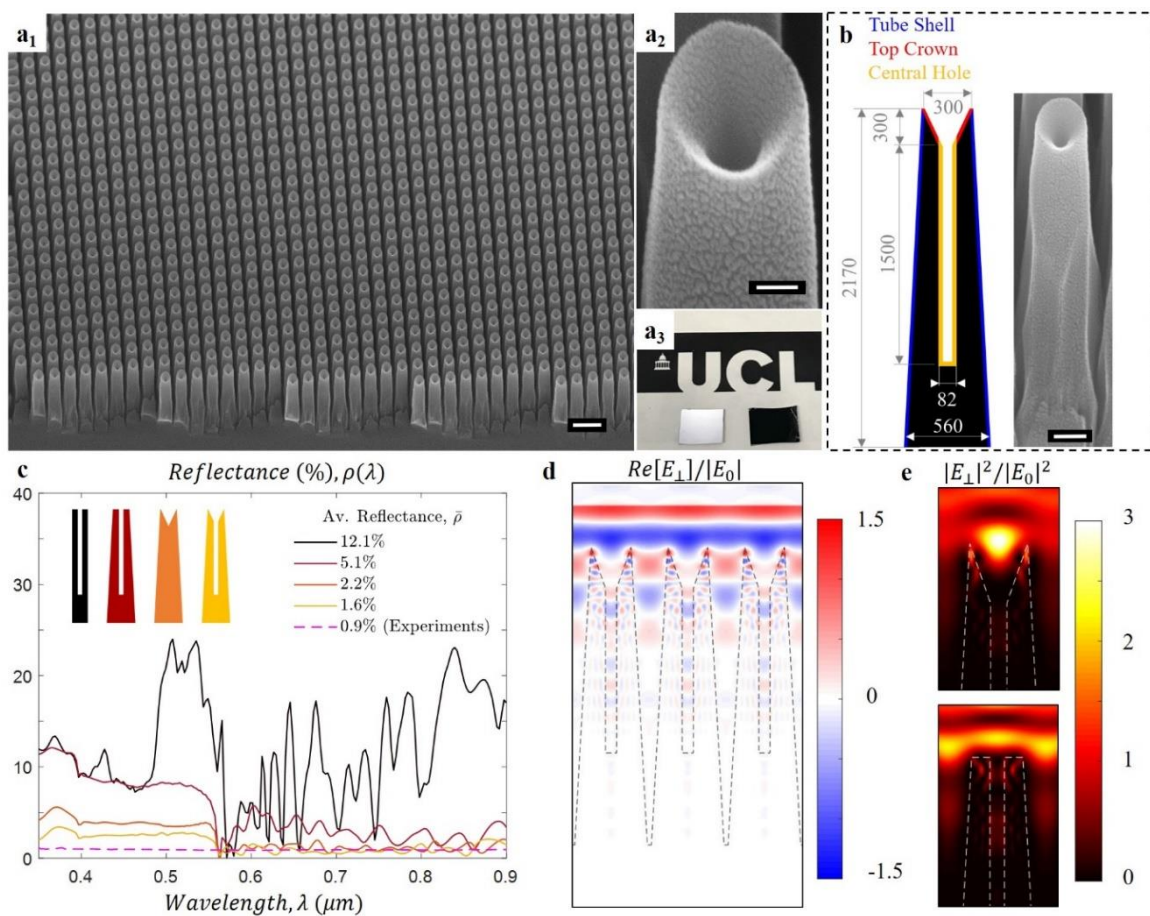


Figure 4. Antireflective study of silicon nanotube arrays. (a₁,a₂) Side view SEM images of the fabricated silicon nanotube arrays highlighting the scale of fabrication (a₁) and crown structure (a₂). (a₃) Photograph of a plain piece of Si (left) next to the sample comprising the crowned-nanotube array (right, ~6 cm²), to visually highlight the ultra-black properties. (b)

Schematic with accompanying SEM image of the nanotube considered in the simulation, together with its overall dimensions (nm). The three main geometrical components of the nanotube (*i.e.*, Tube Shell, Top Crown and Central Hole) are highlighted in the figure for reference. c, Reflectance at normal incidence as obtained from measurements (magenta dashed line), and simulations for four different geometries: straight-walled tube (black curve), tapered tube (red curve), tapered pillar with a top crown (orange curve), and tapered tube with a top crown (yellow curve). (d,e) Distribution of the electric field perpendicular to the plane of incidence (E_{\perp}) for a planewave at 400 nm wavelength and normal incidence. (d) Real part of the normalised electric field ($Re[E_{\perp}]/|E_0|$) for crowned tapered tube arrays. (e) Normalised electric field energy density ($|E_{\perp}|^2/|E_0|^2$) at the tip of a crowned tapered tube (upper) and regular tapered tube (lower). Scale bars: $a_1 = 1 \mu\text{m}$, $a_2 = 100 \text{ nm}$, $b = 200 \text{ nm}$.

CONCLUSION

In this work, we present spacer defined intrinsic multiple patterning as an enabling platform technology for the fabrication of nanotube arrays with independent control of the overall geometries. The versatility of SDIMP stems from the vast availability of photolithographic and self-assembly methods for initial patterning, and numerous target material-spacer pairs of high etching contrast at various RIE processes. This allows for nearly no limit on feature dimensions and spatial arrangement (periodic or not), as well as on material choice, enabling tunable and high-quality structures, evidenced by the photonic properties of the ‘crowned’ nanotube array. Further, as a proof-of-concept, we advance the structural complexity through

an additional iteration, and envision many far-reaching applications spanning metamaterials, wettability, biotechnology, and sensing amongst others.

METHODS

Nanotube fabrication through one SDIMP iteration. The fabrication process flow is provided in Figure 1. First, silicon wafer (MicroChemicals) was cleaned with acetone *via* sonication and subsequently washed with isopropanol. SiO₂ layer (70 nm or 100 nm) was deposited on Si *via* plasma enhanced chemical vapor deposition (PECVD; STPS Multiplex) under low frequency RF with SiH₄ and O₂ vapor at 300°C.

(Step 1) An initial photoresist pattern (holes or pillars) was generated by laser interference lithography (LIL) using a Lloyd's mirror interferometer set up (see Supporting Methods and Figure S5). A primer layer (TI Prime, Microchemicals) was first applied *via* spin-coating (6,000 rpm for 30s and baked at 120°C for 90 s) in order to improve resist adhesion. Photoresist (ma-N 405, Microresist technology) was diluted 1:1 with MIBK (4-methyl-2-pentanone) and spin coated onto the wafer at 3,000 rpm for 30s. Soft baking was carried out in an oven at 100°C (3 min). Square- or hexagonally-packed pillars or holes were generated by means of one or two mirrors using the free-space UV-laser with beam diameter of ~1 mm (IK3201R-F by Kimmon; Class 3B; 25 mW; 325 nm; CW; single mode TEM00). After exposure (pillars; 60 s, holes; 90 s), the photoresist was developed using AZ 726 MIF (Microchemicals) for 30 s. After the pattern was established, a brief oxygen breakthrough was applied to expose underlying material (SiO₂ – hard mask) to be etched (see Table S2-3 for conditions/times).

To generate initial PR pattern, virtually any technique can be employed. In this study, alternatively, UV nanoimprint lithography (NIL) was utilised (for details see Methods – NIL).

(Step 2) To register the PR pattern into the hard mask, reactive ion etching (RIE) was conducted using CHF_3/Ar plasma at temperature of 20°C (PlasmaPro NGP80 RIE, Oxford instruments). After etching, residual PR was removed by O_2 RIE.

(Step 3) Using the hard mask, the pattern was transferred into the underlying Si layer by means of Advanced Silicon Etcher (ASE, STS MESC Multiplex ICP) using Cl plasma. Typically, etching was performed until mask consumption. Note, excessive SiO_2 mask on Si can be removed by hydrofluoric acid (HF). Detailed etching conditions for both RIE processes (Steps 2-3) to generate each nanostructure are listed in Tables S2-S4.

(Step 4) Prior to atomic layer deposition (ALD) of Al_2O_3 spacer, the surfaces were subjected to an RCA cleaning process to remove organic and ionic contaminants. Subsequently, the deposition of Al_2O_3 was conducted in Savannah G2 S200 (Ultratech), using alternating exposures of trimethylaluminum (97%, Aldrich) and deionised water at 200°C with N_2 gas purge steps in between. The exposure and purge time for both precursors used in this study were 0.015 s and 3 s, respectively. Ten cycles of the process equal 1 nm (see Table S2 for deposition thickness).

(Step 5) The breakthrough etch was conducted using Cl plasma (Table S2,S4) to remove the horizontal deposition (equivalent to the deposition thickness; 10 nm/min) whilst revealing vertically aligned spacer mask.

(Step 6) The subsequent etch was continued using Cl plasma (Tables S2,S4) either until spacer mask depletion or until the desired height was reached. The remaining Al₂O₃ mask was removed by HF.

For nanotube fabrication in glass please refer to Supporting Methods.

Complex nanostructures fabrication through two SDIMP iterations. The fabricated single nanotubes were cleaned according to the RCA cleaning process, and placed in the ALD chamber. The second ALD and etch were performed as described before.

For concentric nanotubes (Figure 3b), PR pillars (P = 350 nm) were generated atop of Si with deposited 70 nm of SiO₂ layer. The primer layer and negative-tone PR were applied as described above (Step 1). The Lloyd's set up comprised of one mirror, and the sample was rotated 90° after each exposure (30 s). Development was performed in undiluted AZ-MIF-726 for 90 s. To register the PR nanopillars into the SiO₂ hard mask, RIE was performed (Oxford instruments) with CHF₃/Ar plasma for 90 s. To transfer the pattern from hard mask to Si, RIE (STS) was performed using Cl plasma for 3 min (for both RIE conditions – see Table S3). The sample was cleaned and placed in the ALD chamber, where 40 nm of Al₂O₃ was deposited. Subsequently, the sample was subjected to RIE with Cl plasma for 7 min, at which point it was cleaned and placed back into ALD chamber for a further 25 nm of Al₂O₃ deposition. The final etch was performed for 11.5 min under Cl plasma.

For fabrication of the other demonstrated complex nanostructures through two iterations, please refer to Table S7; the process only differs in etching time and deposition thickness.

Characterisation. Scanning electron microscopy (SEM) was performed using a Field Emission Zeiss Ultra Plus scanning electron microscope with a Gemini column operating at an accelerating voltage of 2-20 kV. Glass samples were coated with a thin layer of gold *via* sputter deposition to minimize charging. ImageJ (<https://imagej.nih.gov/ij/>) was used for statistical analysis of the nanostructure dimensions such as pitch, height, diameters. Additionally, roundness of some structures was characterized ($roundness = \frac{4 \cdot A}{\pi \cdot a^2}$, where A is the surface area and a is major axis; ImageJ) to describe feature shape and compare uniformity.

Soft lithography. The mold substrate was functionalised with a PDMS brush layer as described above, in order to ease separation. Preparation of the poly(urethane acrylate) (PUA) solution was carried out according to a previously reported method.⁴¹ Briefly, the PUA solution was prepared by thorough mixing of 30 wt% of trimethylolpropane ethoxylate triacrylate (409073, Sigma) with respect to the diacrylate prepolymer (Ebecryl 284, Allnex). Subsequently, photo initiators Irgacure 184 (1-Hydroxy-cyclohexyl-phenyl-ketone, 30472119, BASF) and Darocur (2-Hydroxy-2-methylpropiophenone, 405655, Sigma) were added at 1.5 wt% with respect to the combined weight. Finally, a releasing agent (TEGO® Rad 2200N) was added at 1 wt%. The prepared solution was mixed and degassed, and stored in a refrigerator protected from light. The sample was drop casted with the solution and cured for 20 s under a high intensity UV laser (365 nm, CS2010 UV Curing System, ThorLabs), followed by 10-hour curing under low intensity UV light.

NIL. Having generated a pattern with the desired pitch and orientation *via* LIL, and transferred this into Si, NIL was employed to facilitate quick and reproducible pattern replication into PR for further substrates. To generate a positive-tone replica of the pattern, a two-step nanoimprint was conducted. The NIL process was performed on EITRE® 3 (Obducat). Prior to imprinting, the master mold was functionalised with polydimethylsiloxane (PDMS) brush layer according to a previously reported method,⁴² to facilitate a demolding process. Briefly, oxygen plasma was applied to activate the surface which was subsequently grafted with short chain PDMS using 1:10:0.27 v/v/v ratio of dimethyldimethoxysilane : isopropanol : H₂SO₄ (>95%) mixture. The substrate was placed on a hot plate (75°C) and the solution was drop casted atop for 15 s, followed by washing with deionised water, isopropanol and toluene. The intermediate polymer (IPS, Obducat) stamping process was operated at 145°C and 20 bar for 20 s. Transfer of the negative pattern into the photoresist (STU-7, Obducat) was operated at 70°C and 40 bar for 240 s with 120 s of UV curing. For further details on nanotubes replicated *via* NIL and soft lithography please refer to Supporting Methods.

Ultraviolet – visible light spectroscopy measurements. Reflection measurements were taken at 8° off normal incidence. The sample was attached to a port of an integrating sphere (Labsphere) and illuminated using a white light source (KI-120 Koehler Illuminator, Labsphere). Light levels were measured using a fibre coupled spectrometer (QEPro, Ocean Optics) and calibrated against a diffuse reflectance standard (SRS-02-10, Spectralon, Labsphere).

Optical Simulation. Numerical simulations at normal incidence and electric field distribution (Figure 4) were obtained from Finite Difference Time Domain (FDTD) method, using FDTD 3D Electromagnetic Simulator, Lumerical Inc. (<https://www.lumerical.com/products/fdtd/>). Optical properties at oblique angle of incidence (Figure S14), were obtained from Rigorous Coupled Wave Analysis (RCWA) method using the software package S4.⁴³ In all the simulations, periodic boundary conditions on a square lattice were considered, and the power flux was monitored above and below the nanotubes structure to quantify reflection and transmission, respectively. The refractive index of silicon was obtained from a previous report.⁴⁴

ASSOCIATED CONTENT

The authors declare no competing financial interest.

Supporting Information

The Supporting Information is available free of charge online. The manuscript is accompanied by: (i) Supporting Methods which elaborate on LIL; fabrication in glass; and replication processes in polymers. (ii) Supporting Text (Text S1-S2) referring to future outlook spanning fabrication and applications. (iii) Supporting Figures (Figure S1-S13) which provide additional schematics (explaining in details fabrication routes), SEMs, AFMs, experimental setups, and optical properties of the tapered nanotube with a top crown at oblique angle of incidence. (iv) Supporting Tables (Tables S1-S7) which detail fabrication conditions for both SDIMP iterations; tunability at each SDIMP step; and further dimensions of some nanostructures.

AUTHOR INFORMATION

Corresponding Author

* Ioannis Papakonstantinou – Photonic Innovations Lab, Department of Electronic & Electrical Engineering, University College London, Torrington Place, London WC1E 7JE, UK; Email: i.papakonstantinou@ucl.ac.uk

Author Contributions

‡ These authors contributed equally.

T.L. and I.P. conceived the project. T.L., S.K.L. and M.M. carried out structure fabrication and imaging. S.K.L. prepared the data with help from M.M and J.O.. S.K.L. and M.M. drafted the manuscript with help from I.P.. M.P. and I.P. conducted the optical measurements. F.R. performed the optical simulations and calculations. I.P., I.P.P., M.K.T. and I.G.T. facilitated the research. All authors contributed to the discussion and revision of the manuscript.

ACKNOWLEDGEMENTS

The work was conducted in the framework of the European Research Council (ERC) starting grant IntelGlazing, grant no: 679891. We are grateful to Lloyd's Register Foundation for an International Consortium of Nanotechnology (ICON) research grant and UCL BEAMS School for a PhD studentship. Funding by the ERC grant NICEDROPS, grant no: 714712 is also gratefully acknowledged. We acknowledge the invaluable support of the James Watt Nanofabrication Centre at the University of Glasgow and we would particularly like to thank

M. Dragsnes and his technical team for their contributions. Finally, we acknowledge the assistance of the technical team in the London Centre for Nanotechnology (LCN).

REFERENCES

- (1) Liu, C.; Gillette, E. I.; Chen, X.; Pearse, A. J.; Kozen, A. C.; Schroeder, M. A.; Gregorczyk, K. E.; Lee, S. B.; Rubloff, G. W. An All-In-One Nanopore Battery Array. *Nat. Nanotechnol.* **2014**, *9*, 1031–1039.
- (2) Wallentin, J.; Anttu, N.; Asoli, D.; Huffman, M.; Aberg, I.; Magnusson, M. H.; Siefer, G.; Fuss-Kailuweit, P.; Dimroth, F.; Witzigmann, B.; Xu, H. Q.; Samuelson, L.; Deppert, K.; Borgstrom, M. T. InP Nanowire Array Solar Cells Achieving 13.8% Efficiency by Exceeding the Ray Optics Limit. *Science*. **2013**, *339*, 1057–1060.
- (3) Rahman, A.; Ashraf, A.; Xin, H.; Tong, X.; Sutter, P.; Eisaman, M. D.; Black, C. T. Sub-50-Nm Self-Assembled Nanotextures for Enhanced Broadband Antireflection in Silicon Solar Cells. *Nat. Commun.* **2015**, *6*, 5963.
- (4) Gibson, S. J.; van Kasteren, B.; Tekcan, B.; Cui, Y.; van Dam, D.; Haverkort, J. E. M. M.; Bakkers, E. P. A. M. A. M.; Reimer, M. E. Tapered InP Nanowire Arrays for Efficient Broadband High-Speed Single-Photon Detection. *Nat. Nanotechnol.* **2019**, *14*, 473–479.
- (5) Chu, K.-H.; Xiao, R.; Wang, E. N. Uni-Directional Liquid Spreading on Asymmetric Nanostructured Surfaces. *Nat. Mater.* **2010**, *9*, 413–417.
- (6) Wen, L.; Xu, R.; Mi, Y.; Lei, Y. Multiple Nanostructures Based on Anodized Aluminium Oxide Templates. *Nat. Nanotechnol.* **2017**, *12*, 244–250.

- (7) Das Gupta, T.; Martin-Monier, L.; Yan, W.; Le Bris, A.; Nguyen-Dang, T.; Page, A. G.; Ho, K.-T.; Yesilköy, F.; Altug, H.; Qu, Y.; Sorin, F. Self-Assembly of Nanostructured Glass Metasurfaces *via* Templated Fluid Instabilities. *Nat. Nanotechnol.* **2019**, *14*, 320–327.
- (8) Kuznetsov, A. I.; Miroshnichenko, A. E.; Brongersma, M. L.; Kivshar, Y. S.; Luk'yanchuk, B. Optically Resonant Dielectric Nanostructures. *Science.* **2016**, *354*, aag2472.
- (9) Jeong, H.; Song, H.; Pak, Y.; Kwon, I. K.; Jo, K.; Lee, H.; Jung, G. Y. Enhanced Light Absorption of Silicon Nanotube Arrays for Organic/Inorganic Hybrid Solar Cells. *Adv. Mater.* **2014**, *26*, 3445–3450.
- (10) Song, T.; Xia, J.; Lee, J.-H.; Lee, D. H.; Kwon, M.-S.; Choi, J.-M.; Wu, J.; Doo, S. K.; Chang, H.; Park, W. Il; Zang, D. S.; Kim, H.; Huang, Y.; Hwang, K.-C.; Rogers, J. A.; Paik, U. Arrays of Sealed Silicon Nanotubes As Anodes for Lithium Ion Batteries. *Nano Lett.* **2010**, *10*, 1710–1716.
- (11) Park, M.-H.; Kim, M. G.; Joo, J.; Kim, K.; Kim, J.; Ahn, S.; Cui, Y.; Cho, J. Silicon Nanotube Battery Anodes. *Nano Lett.* **2009**, *9*, 3844–3847.
- (12) Wang, M.; Iocozia, J.; Sun, L.; Lin, C.; Lin, Z. Inorganic-Modified Semiconductor TiO₂ Nanotube Arrays for Photocatalysis. *Energy Environ. Sci.* **2014**, *7*, 2182–2202.
- (13) Fan, R.; Wu, Y.; Li, D.; Yue, M.; Majumdar, A.; Yang, P. Fabrication of Silica Nanotube Arrays from Vertical Silicon Nanowire Templates. *J. Am. Chem. Soc.* **2003**, *125*, 5254–5255.
- (14) La Rocca, R.; Messina, G. C.; Dipalo, M.; Shalabaeva, V.; De Angelis, F. Out-Of-

- Plane Plasmonic Antennas for Raman Analysis in Living Cells. *Small* **2015**, *11*, 4632–4637.
- (15) Messina, G. C.; Dipalo, M.; La Rocca, R.; Zilio, P.; Caprettini, V.; Proietti Zaccaria, R.; Toma, A.; Tantussi, F.; Berdondini, L.; De Angelis, F. Spatially, Temporally, and Quantitatively Controlled Delivery of Broad Range of Molecules into Selected Cells through Plasmonic Nanotubes. *Adv. Mater.* **2015**, *27*, 7145–7149.
- (16) Chen, J.-K.; Chen, W.-T.; Cheng, C.-C.; Yu, C.-C.; Chu, J. P. Metallic Glass Nanotube Arrays: Preparation and Surface Characterizations. *Mater. Today* **2018**, *21*, 178–185.
- (17) Li, J.; Liu, W.; Wang, J.; Rozen, I.; He, S.; Chen, C.; Kim, H. G.; Lee, H.-J.; Lee, H.-B.-R.; Kwon, S.-H.; Li, T.; Li, L.; Wang, J.; Mei, Y. Nanoconfined Atomic Layer Deposition of TiO₂/Pt Nanotubes: Toward Ultrasmall Highly Efficient Catalytic Nanorockets. *Adv. Funct. Mater.* **2017**, *27*, 1700598.
- (18) Heo, C.-J.; Kim, S.-H.; Jang, S. G.; Lee, S. Y.; Yang, S.-M. Gold “Nanogrills” with Tunable Dipolar Multiple Plasmon Resonances. *Adv. Mater.* **2009**, *21*, 1726–1731.
- (19) Zhang, J.; Li, Y.; Zhang, X.; Yang, B. Colloidal Self-Assembly Meets Nanofabrication: From Two-Dimensional Colloidal Crystals to Nanostructure Arrays. *Adv. Mater.* **2010**, *22*, 4249–4269.
- (20) Xu, X.; Yang, Q.; Wattanatorn, N.; Zhao, C.; Chiang, N.; Jonas, S. J.; Weiss, P. S. Multiple-Patterning Nanosphere Lithography for Fabricating Periodic Three-Dimensional Hierarchical Nanostructures. *ACS Nano* **2017**, *11*, 10384–10391.
- (21) Davis, A. L.; Nijhout, H. F.; Johnsen, S. Diverse Nanostructures Underlie Thin Ultra-Black Scales in Butterflies. *Nat. Commun.* **2020**, *11*, 1294.

- (22) De Angelis, F.; Malerba, M.; Patrini, M.; Miele, E.; Das, G.; Toma, A.; Zaccaria, R. P.; Di Fabrizio, E. 3D Hollow Nanostructures as Building Blocks for Multifunctional Plasmonics. *Nano Lett.* **2013**, *13*, 3553–3558.
- (23) Mackus, A. J. M.; Bol, A. A.; Kessels, W. M. M. The Use of Atomic Layer Deposition in Advanced Nanopatterning. *Nanoscale* **2014**, *6*, 10941–10960.
- (24) Dallorto, S.; Staaks, D.; Schwartzberg, A.; Yang, X.; Lee, K. Y.; Rangelow, I. W.; Cabrini, S.; Olynick, D. L. Atomic Layer Deposition for Spacer Defined Double Patterning of Sub-10 Nm Titanium Dioxide Features. *Nanotechnology* **2018**, *29*, 405302.
- (25) Liu, C.-C.; Franke, E.; Mignot, Y.; Xie, R.; Yeung, C. W.; Zhang, J.; Chi, C.; Zhang, C.; Farrell, R.; Lai, K.; Tsai, H.; Felix, N.; Corliss, D. Directed Self-Assembly of Block Copolymers for 7 Nanometre FinFET Technology and Beyond. *Nat. Electron.* **2018**, *1*, 562–569.
- (26) Moon, H.-S.; Kim, J. Y.; Jin, H. M.; Lee, W. J.; Choi, H. J.; Mun, J. H.; Choi, Y. J.; Cha, S. K.; Kwon, S. H.; Kim, S. O. Atomic Layer Deposition Assisted Pattern Multiplication of Block Copolymer Lithography for 5 Nm Scale Nanopatterning. *Adv. Funct. Mater.* **2014**, *24*, 4343–4348.
- (27) Wan, Z.; Lee, H. J.; Kim, H. G.; Jo, G. C.; Park, W. I.; Ryu, S. W.; Lee, H.-B.-R.; Kwon, S.-H. Circular Double-Patterning Lithography Using a Block Copolymer Template and Atomic Layer Deposition. *Adv. Mater. Interfaces* **2018**, *5*, 1800054.
- (28) Henry, M. D.; Walavalkar, S.; Homyk, A.; Scherer, A. Alumina Etch Masks for Fabrication of High-Aspect-Ratio Silicon Micropillars and Nanopillars.

- Nanotechnology* **2009**, *20*, 255305.
- (29) Williams, K. R.; Gupta, K.; Wasilik, M. Etch Rates for Micromachining Processing - Part II. *J. Microelectromechanical Syst.* **2003**, *12*, 761–778.
- (30) Chung, C.-K. Geometrical Pattern Effect on Silicon Deep Etching by an Inductively Coupled Plasma System. *J. Micromechanics Microengineering* **2004**, *14*, 656–662.
- (31) Wu, B.; Kumar, A.; Pamarthy, S. High Aspect Ratio Silicon Etch: A Review. *J. Appl. Phys.* **2010**, *108*, 051101.
- (32) Yoo, D.; Gurunatha, K. L.; Choi, H. K.; Mohr, D. A.; Ertsgaard, C. T.; Gordon, R.; Oh, S. H. Low-Power Optical Trapping of Nanoparticles and Proteins with Resonant Coaxial Nanoaperture Using 10 Nm Gap. *Nano Lett.* **2018**, *18*, 3637–3642.
- (33) Nagpal, P.; Lindquist, N. C.; Oh, S.-H.; Norris, D. J. Ultrasoother Patterned Metals for Plasmonics and Metamaterials. *Science.* **2009**, *325*, 594–597.
- (34) Zhu, J.; Yu, Z.; Burkhard, G. F.; Hsu, C.-M.; Connor, S. T.; Xu, Y.; Wang, Q.; McGehee, M.; Fan, S.; Cui, Y. Optical Absorption Enhancement in Amorphous Silicon Nanowire and Nanocone Arrays. *Nano Lett.* **2009**, *9*, 279–282.
- (35) Brongersma, M. L.; Cui, Y.; Fan, S. Light Management for Photovoltaics Using High-Index Nanostructures. *Nat. Mater.* **2014**, *13*, 451–460.
- (36) Boden, S. A.; Bagnall, D. M. Tunable Reflection Minima of Nanostructured Antireflective Surfaces. *Appl. Phys. Lett.* **2008**, *93*, 133108.
- (37) Garnett, E.; Yang, P. Light Trapping in Silicon Nanowire Solar Cells. *Nano Lett.* **2010**, *10*, 1082–1087.
- (38) Huang, Y. F.; Chattopadhyay, S.; Jen, Y. J.; Peng, C. Y.; Liu, T. A.; Hsu, Y. K.; Pan,

- C. L.; Lo, H. C.; Hsu, C. H.; Chang, Y. H.; Lee, C. S.; Chen, K. H.; Chen, L. C. Improved Broadband and Quasi-Omnidirectional Anti-Reflection Properties with Biomimetic Silicon Nanostructures. *Nat. Nanotechnol.* **2007**, *2*, 770–774.
- (39) Yang, J.; Luo, F.; Kao, T. S.; Li, X.; Ho, G. W.; Teng, J.; Luo, X.; Hong, M. Design and Fabrication of Broadband Ultralow Reflectivity Black Si Surfaces by Laser Micro/Nanoprocessing. *Light Sci. Appl.* **2014**, *3*, e185.
- (40) Fan, Z.; Kapadia, R.; Leu, P. W.; Zhang, X.; Chueh, Y. L.; Takei, K.; Yu, K.; Jamshidi, A.; Rathore, A. A.; Ruebusch, D. J.; Wu, M.; Javey, A. Ordered Arrays of Dual-Diameter Nanopillars for Maximized Optical Absorption. *Nano Lett.* **2010**, *10*, 3823–3827.
- (41) Choi, S.-J.; Yoo, P. J.; Baek, S. J.; Kim, T. W.; Lee, H. H. An Ultraviolet-Curable Mold for Sub-100-Nm Lithography. *J. Am. Chem. Soc.* **2004**, *126*, 7744–7745.
- (42) Wang, L.; McCarthy, T. J. Covalently Attached Liquids: Instant Omniphobic Surfaces with Unprecedented Repellency. *Angew. Chem. Int.* **2016**, *55*, 244–248.
- (43) Liu, V.; Fan, S. S4 : A Free Electromagnetic Solver for Layered Periodic Structures. *Comput. Phys. Commun.* **2012**, *183*, 2233–2244.
- (44) Green, M. A. Self-Consistent Optical Parameters of Intrinsic Silicon at 300K Including Temperature Coefficients. *Sol. Energy Mater. Sol. Cells* **2008**, *92*, 1305–1310.

Table of Contents

